Overview on thermoactive materials, simulations and applications

Liliana Fernandes[1], Eduardo Fernández[1], Pedro Martins[2,3], Nelson Ferreira[4], Paulo Antunes[4] and Senentxu Lanceros-Mendez[1,5]

1. BCMaterials, Basque Centre for Materials and Applications, UPV/EHU Science Park, 48940 Leioa, Spain
2. Centro/Departamento de Física, University of Minho, Braga 4710-057, Portugal
3. IB-S Institute of Science and Innovation for Sustainability, Universidade do Minho, 4710-057, Braga, Portugal
4. Critical Materials S.A., Avepark - Science and Technology Park, Guimarães, Portugal
5. IKERBASQUE, Basque Foundation for Science, 48013 Bilbao, Spain

Abstract

Thermoelectric (TE) materials have been attracting increasing interest once they are capable of directly convert temperature variations into electricity, being used in thermoelectric generators and thermoelectric sensor devices, among others.

This work reports on the main principles of thermoelectric and thermomagnetic effects as well as the main materials used for the development of applications. Additionally, recent advances in the design and properties of thermoelectric materials, modelling approaches and some relevant applications are presented.

1. Introduction: Thermoelectric and thermomagnetic effect

The thermoelectric and thermomagnetic theory phenomena in metals was developed in 1930 -1950 and it is based on a kinetic approach [1], where transport equations are

formulated and solved for different systems in order to obtain the transport coefficients that characterize the thermoelectric and thermomagnetic effects [2].

Thermoelectric phenomena were firstly discovered by Thomas J. Seebeck, who observed that a compass needle would be deflected by a closed loop formed by two different metals joined in two places, with a temperature difference (ΔT) between the joints [3]. This effect, observed in metals and semiconducting materials, illustrates the coupling of two thermodynamic entities: the electrochemical potential and the temperature (Figure 1a) [4].
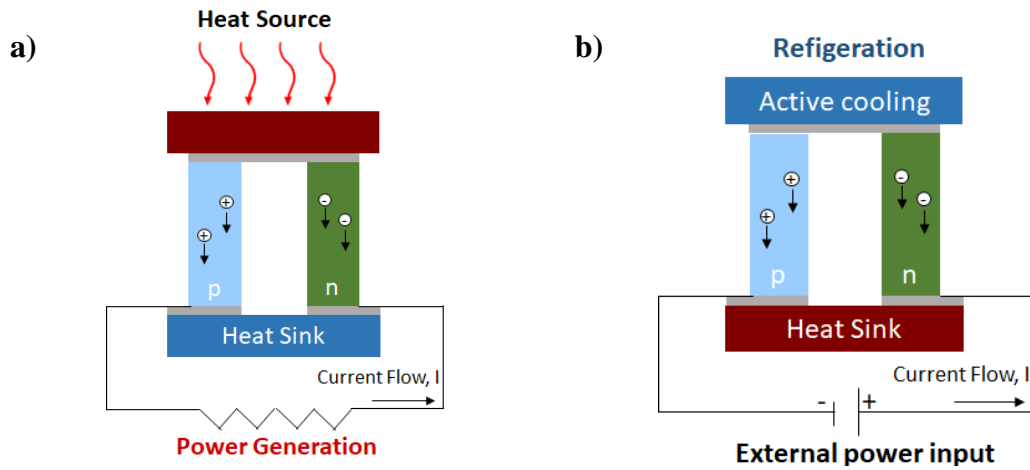
Figure 1. Illustration of how a thermoelectric semiconducting material can: a) convert heat directly to electricity (Seebeck effect); b) heat up or cool down at an electrified junction (Peltier effect).

Thermoelectric devices have found many applications that include temperature sensing, solid-state heating/cooling and direct energy conversion from wasted heat [5].

When a metallic bar is subjected to a voltage (V) or a temperature difference (ΔT), an electric current is generated. For small voltages and temperature gradients we may assume, in the absence of a magnetic field, a linear relation between the electric current density J and the voltage gradients (Ohm's law) [6]:

$$J^E = \sigma(-\nabla V) + \alpha(-\nabla T) = \sigma E - \alpha \nabla T \qquad (1)$$

where $E \equiv -\nabla V$ is the electric field, σ the electrical conductivity and α is the

thermoelectric coefficient. If the edges of the conducting bar are maintained at different temperatures at steady state, no electric current flows ($J^E = 0$). Thus, from Equation (1), it is obtained:

$$\sigma E_S - \alpha \nabla T = 0 \tag{2}$$

where E_S is the electric field generated by the thermal electromotive force (emf). The Seebeck coefficient (thermoelectric power) S is then defined as the electric field generated by a thermal gradient in the absence of a charge current and is defined through:

$$E_S = S \nabla T, \qquad S \equiv \frac{\alpha}{\sigma} = \frac{E_S}{\nabla T} \tag{3}$$

The electrical conductivity σ is positive, but the Seebeck coefficient S can be positive or negative. Based in the classical statistical idea that different temperatures generate different electron drift velocities, it is obtained:

$$S = -\frac{c_V}{3ne} \tag{4}$$

where c_V is the heat capacity per unit volume and n the electron density. Setting c_V equal to $\frac{3nk_B}{2}$, the classical formula for thermopower is obtained, according to the Drude model:

$$S_{classical} = -\frac{k_B e}{2} = -43 \; \mu V K^{-1} \tag{5}$$

However, this model does not correspond to the measured experimental values which are ~100 times smaller than $S_{classical}$ [7]. With the Sommerfeld expansion though, the theoretical value of the thermopower is much closer to the experimental one, being defined as [7]:

$$S = -\frac{c_v}{3ne} = \frac{\pi^2}{6}\left(\frac{k_B}{e}\right)\left(\frac{k_B T}{\varepsilon_F}\right) \sim \frac{k_B T}{\varepsilon_F} \times 10^{-4} \; V K^{-1} \tag{6}$$

Meanwhile Jean C. A. Peltier discovered the inverse effect, that under isothermal conditions an electrical current can cause a temperature variation at the junction[8] (Figure 1).

The Peltier effect (Figure 1b) describes the heat at an electrified junction of two different materials. The Peltier coefficients, Π, represent how much heat flow is carried per unit of charge through a given material [9]. Since charge current must be continuous across a junction, the associated heat flow will develop a discontinuity if the Peltier coefficients of the two materials are different. Depending on the magnitude of the current, heat must accumulate or dissipate at the junction due to a non-zero divergence, caused by the carriers attempting to return to the equilibrium that existed before the current was applied by transferring energy from one connector to another [2]. The Peltier effect can be then represented as:

$$q = \Pi_{AB}I \tag{7}$$

with q being the heat flux, I the electrical current and Π_{AB} the Peltier coefficient of materials A and B. With the Osanger relations, more specifically with the Kelvin relations [10, 11] this effect can be related to the Seebeck coefficient,

$$\Pi_{AB} = S_{AB}T \tag{8}$$

and considering metallic anisotropic crystalline structure it can also be written in terms of the electrical and thermal conductivity (γ). Considering the thermal flux Equation (9):

$$q = \sigma E_s + \gamma \nabla T \tag{9}$$

and recalling the Seebeck coefficient from (3) it becomes:

$$q = \nabla T(-\sigma S^2 T + \gamma) \tag{10}$$

Since the second term is much larger than the first one, Equation (10) can be simplified as follows:

$$q = \nabla T \gamma \tag{11}$$

Finally, combining equations (9) and (12), the Peltier coefficient can be written as:

$$\Pi = \frac{\alpha}{\sigma}T \tag{12}$$

The kinetic coefficients can also be related by the Wiedemann-Franz law:

$$\frac{\gamma}{\sigma} = LT \tag{13}$$

where L is the Lorentz number and can be written as: $L = \frac{\pi^2 k_B^2}{3e^2}$ [6].

For the Thomson effect, an electric current flows along a single conductor with a temperature gradient, then an energy interaction takes place in which power is either absorbed or emitted, depending on the direction of the current and gradient, describing the heating and cooling of a material when a current passes through it [12]. The Seebeck effect is, therefore, the result of both the Peltier and Thomson effects. This combined effect can be written as:

$$\dot{q} = -KJ \cdot \nabla T \tag{14}$$

where K is the Thomson coefficient and $\dot{q}$ is the heat production rate. Another Kelvin relation links the Thomson with the Seebeck coefficient as [9]:

$$K = T\frac{dS}{dT} \tag{15}$$

While moving in a magnetic field, electric charges are exposed to transverse forces and thermoelectric effects will arise. Thus, thermomagnetic effects are caused by the action of a magnetic field on moving electric charges: electrons in conductors, and electrons and holes in semiconductors. The Seebeck and Peltier effects will have corresponding thermomagnetic effects, the Nernst $|N|$ and Ettinghausen $|P|$ effects [13].

The Nernst effect is the thermal equivalent of the Hall effect, describing the appearance of a transverse voltage (dV/dy) resulting from the presence of a magnetic field (H_z) and a longitudinal temperature gradient (dT/dx) [14]:

$$|N| = \frac{dV/dy}{H_z \, dT/dx} \tag{16}$$

From a transverse magnetic field (H_z) and a longitudinal electric current flow results a temperature gradient (dT/dy), and so, the Ettingshausen coefficient can be written as:

$$|P| = \frac{dT/dy}{i_x H_z} \tag{17}$$

where i_x is the longitudinal current density [13]. Just like with the Seebeck and Peltier effects, the Nernst and Ettingshausen effects are related. The thermodynamic relation between the Nernst and Ettingshausen coefficients, also known as the Bridgman relation [11] can be represented by:

$$P\gamma = NT \tag{18}$$

The thermal conductivity must be included due to the definition of the Ettingshusen coefficient in temperature gradient instead of heat flow [15].

If a longitudinal temperature gradient ($\frac{dT}{dx}$) and a transverse magnetic field H_z are present, not only a transverse electric field E_y is observed but also a transversal temperature gradient (dT/dy) [13]. This observed effect is called Righi–Leduc effect, and the corresponding coefficient $|S|$ is defined as:

$$|S| = \frac{dT/dy}{H_z \, dT/dx}. \tag{19}$$

2. Major drivers of thermoelectric and thermomagnetic effects

In the following, the major contributions that can have relevant influence in the thermoelectric and thermomagnetic effects are introduced.

2.1 Thermal Gradients: obviously, the main driver of thermoelectric and thermomagnetic effects are the thermal gradients that may exist in materials and materials junctions. This will be reflected both at the macro and the microscale. Thus, most theoretical models have been devoted to simulate and theoretically explain the effect of thermal gradients in different materials at different scales [16-19].

A theoretical model for describing effective thermal conductivity (ETC) of nanocrystalline materials has been proposed by Dong, H. *et al.* [16], so that the ETC can be easily obtained from its single crystal thermal conductivity, grain size, the Kaptiza thermal resistance and single crystal phonon mean free path (PMFP). Using a large-scale atomic/molecular massively parallel simulation (LAMMPS) molecular dynamics package, four model sizes with different domain sizes of 40, 80, 120 and 160 Å for models 1, 2, 3 and 4 respectively, and the same grain size are listed in Figure 2, as well as the calculated separate ETCs. The models were developed with the Voronoid method using non- equilibrium molecular dynamics (NEMD) (Figure 2a) with the intragranular atoms in blue atoms and the grain boundary atoms in green.
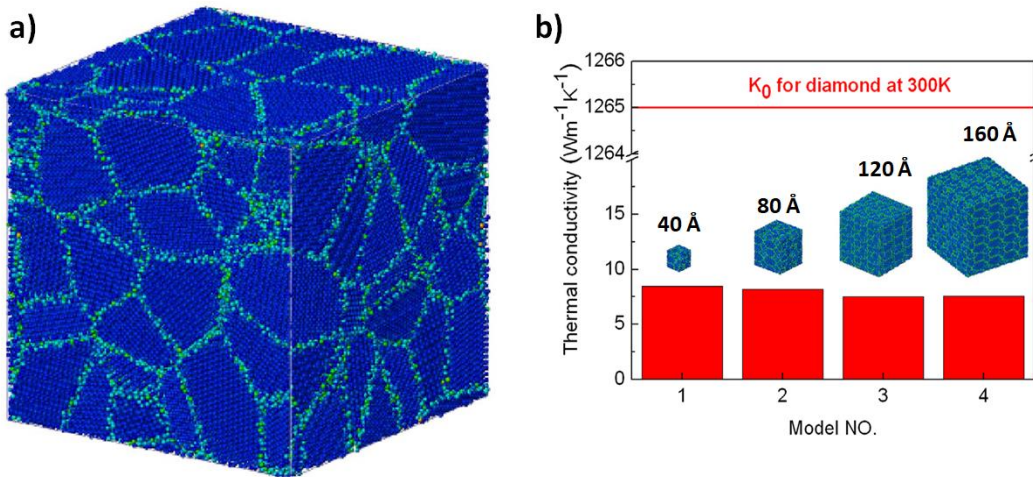

Figure 2. a) Nanocrystalline diamond model example developed by a Voronoi method. The grain boundary atoms are green and; b) model Variation of thermal conductivity for nanocrystalline diamond with different simulation model sizes. **Image adapted with permission from,** [16].

In Figure 2b the variation of the thermal conductivity between the results obtained with these models is very small, although the simulation domain sizes are quite different. Using a different simulation method, COMSOL^{TM}, Zhou *et al.* [17] developed a multiscale theoretical model to analyse promising solutions for enhancing power generated by

Thermoelectric Generators (TEGs), which incorporate water-fed heat exchangers with commercially available thermoelectric modules. The patterned topography (Figure 3) on wall surfaces is implemented and increased device performance can be observed by introducing stirred flows into the heat exchangers and equalizing the temperature across the channels. At a micro scale Zhou *et al.* obtained approximately 30% enhancement in power generation for the base-relief TEG, indicating the need of mixing structures. In addition, by varying the cross-sectional area of a single channel in a conversion capability sense, it is shown that the structured surfaces have a stronger impact on the TEGs at the micro scale, being able to improve the power output by 40%. Finally, it was explored the thermal transport capability of water by loading it with CuO nanoparticles with diameters of 3 and 10 nm, in the TEGs with macro and micro heat exchangers, being obtained a performance superior by 14%. On the other hand, for the macro scale, no improvement was observed.
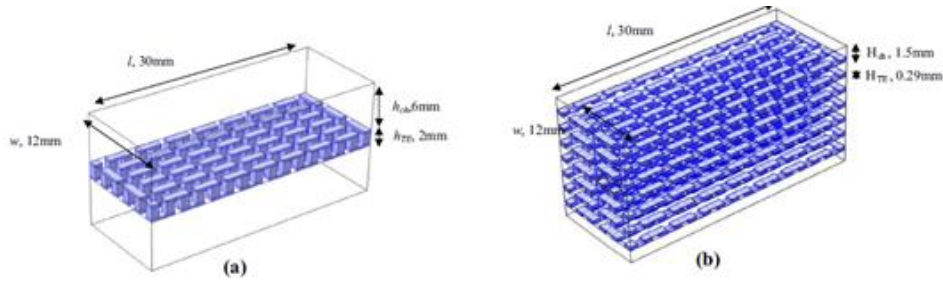

Figure 3. Geometry specifications of the TEG at the: (a) macro scale; (b) micro scale, **Image taken with permission from,** [17].

Also, Mortazavi *et al.* [18] described a multiscale model of the heat conduction in Molybdenum Disulfide (MoS$_2$) films for its application in nanoelectronics using LAMMP molecular dynamics package same as in [16]. Single layer MoS$_2$ membranes were designed being reached advanced heterostructures with tuneable electronic properties. It was also analysed the thermal conductivity by developing a combined atomistic-continuum multiscale model. The properties obtained from the atomistic simulations were then used to develop

macroscopic samples of MoS$_2$ heterostructures using the finite element method. Further, it was reported the possibility of finely tuning the heat transport along MoS$_2$ heterostructures by controlling the domain size and the concentration of the different semiconducting and metallic phases.

2.2 Microstructure: Gao Yuan Wen *et al.* [20] presented a theoretical model and a relevant analysis of the grain size effect on bulk poly-crystalline thermoelectric (PTE) materials based on the Boltzmann transport equation. It was demonstrated that the model can effectively describe the size effect on the Seebeck coefficient, being reported that the Seebeck coefficient increases with decreasing grain size. Further, the size effect on the Seebeck coefficient was related to the transmissivity and the mean free path of electrons (Figure 4).
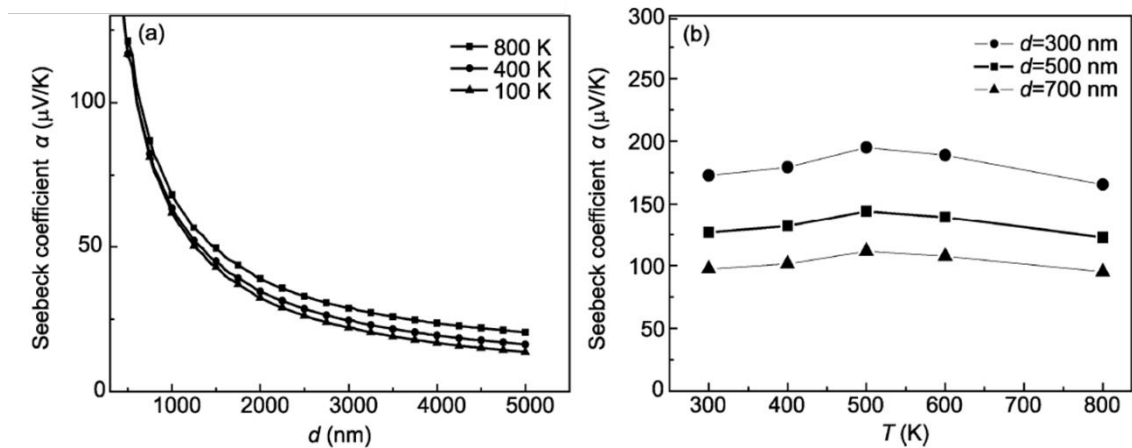
Figure 4. The Seebeck coefficients vs. grain size at different temperatures (a); and the dependence of temperature on the Seebeck coefficient for different grain sizes (b). **Image taken with permission from,** [20].

On the other hand, Trivedi *et al.* [21] performed an experimental approach studying the thermoelectric properties of Ni doped Dy filled CoSb$_3$ skutterudites (Dy$_{0.4}$Co$_{4-x}$Ni$_x$Sb$_{12}$ with x=0, 0.4 and 0.8) showing that with increasing Ni content the lattice thermal conductivity decreased resulting in a higher figure of merit (zT) ~1.4 $\pm$ 0.14 at 773 K for

the sample $Dy_{0.4}Co_{3.2}Ni_{0.8}Sb_{12}$ when compared to ~0.12 ± 0.01 for the $Dy_{0.4}Co_{3.6}Ni_{0.4}Sb_{12}$ sample.

2.3 Magnetic Field: In the thermomagnetic effects, a magnetic field changes the trajectory of moving charges. In particular, it deflects both the electric current flowing through the material and the heat flux associated with the transfer of particles [22]. Thus, magnetic field variations and perturbations will influence the overall thermoelectric (minor influence) and thermomagnetic (major influence) response.

K. Schröder and M Otooni [23] reported a variations in the Seebeck coefficient for copper and in the 1-10 $nV.°C^{-1}$ range for other materials, like copper iron and $Cu_{55}Ni_{45}$ (constantan), under a magnetic field of 27 kOe. Further, M. Murata *et al* [24] tested $Bi_{90}Sb_{10}$, a high performance thermoelectric material at room temperature, and showed an increase in the thermoelectric figure of merit of 37% under a magnetic field of 2.5 T.

2.4 Interface effects: In bulk materials the relevant interfaces are grain boundaries, which separate differently oriented crystals of the same phase, and heterophase interfaces, which separate different materials. In thin-film and nanowire thermoelectric materials, the free surface in contact with vacuum or atmosphere can be of large importance. Interfaces within a thermoelectric materials have been shown to reduce the thermal conductivity, and under certain conditions, to enhance the Seebeck coefficient [25]. However, interfaces also usually increase the electrical resistivity [26]. For a constant γ, improving the zT, requires the proportional reduction in charge carrier mobility resulting from increased interfacial scattering to be less than the corresponding reduction in thermal conductivity [27]. Thus, balancing the electronic and thermal properties of the interfaces is critical to tailor material's properties for optimal thermoelectric performance. The Seebeck coefficient can be changed by the presence

of interfaces due to size effects or energy filtering of the charge carriers [28-31]. It is also related to the energy derivative of the electronic density of states $N(E)$ and the scattering (or relaxation) time τ through the Mott relation (Equation (20)):

$$S = \frac{\pi^2 k_B{}^2 T}{3q} \left(\frac{dlnN(E)}{dE} + \frac{dln\tau(E)v(E)^2}{dE} \right)_{E=E_F} \tag{20}$$

(where v is the electronic group velocity). Quantum size effects can create sharp changes in the electronic density of states that should lead to enhancements in α and increase zT. Increased α and increased zT have also been observed in materials with resonant impurity states. Alternatively, enhancing the energy dependence of $\tau(E)$ by affecting the scattering mechanism will also increase the Seebeck coefficient [32].

Homm *et al.* [25] studied the effects of interface geometry on microstructured ZnO-based thin films using an empirical network model showing a clear dependence of the interface geometry and length. The interfaces length ranged between 5000 µm and 15000 µm and the structures studied were parallel and toothed. The Seebeck coefficient for the studied materials increased with decreasing interface length. Also, Wang *et al.* [26] studied the electrical resistivity of 1000 nm Cu/Ta multilayers, deposited by RF magnetron sputtering onto a polyimide substrate, with a four point probe method and the size of the monolayers ranging from 500 to 10 nm, showing that the electrical resistivity of the multilayer increased with decreasing monolayer size.

It should be noticed that time dependent variations of all aforementioned phenomena will lead to transient and out of equilibrium thermoelectric and thermomagnetic responses.

3. Materials and main material properties

The literature related with thermoelectric materials is usually more concerned with recent advances on materials able to perform with efficiency, energy conversion between heat and

electricity [5]. Thermoelectric energy conversion is an all-solid-state technology used in heat pumps and electrical power generation which are thermodynamically similar to vapour power generation or heat pumping cycles using electrons as the working "fluid" (instead of gases or liquids) [33]. There is available a reasonable database of information related with thermoelectric materials showing a good energy conversion efficiency (5-20%) [34]. These materials are typically alloys, including telluride-based materials (e.g. PbTe, Bi_2Te_3), Si-Ge alloys, rare earth chalcogenides and half-Heusler alloys [35-38]. It is also becoming more usual the enhancement of thermoelectric properties through doping [39, 40], alloying [41, 42] and material nanostructuring [43, 44].

A transversal characteristic of these thermoelectric efficient materials is the intrinsic value of the figure of merit expressed by:

$$zT = \frac{S^2 \sigma T}{\kappa} \tag{21}$$

For ideal thermoelectric materials the zT should be ≥ 1 in order to obtain an energy conversion efficiency larger than 10% [45]. From Equation (21) it is possible to conclude that an ideal thermoelectric material must exhibit:

 i) high electrical conductivity;

ii) large Seebeck coefficient;

 iii) low thermal conductivity.

 In fact, the high Seebeck coefficient contributes to the generation of a high electrical potential/thermovoltage. High electrical conductivity is needed to minimize the Joule heating effect and the low thermal conductivity ensures high temperature gradients. The combination of both requirements is difficult, once they often depend on the intrinsic characteristics of the thermoelectric material such as electrical resistivity and thermal conductivity [46]. Recent efforts on the optimization of the thermoelectric materials performance are related with

decreasing the denominator of Equation (21), by developing materials with modified/tailored morphology in order to decrease the thermal conductivity by scattering phonons [33].

In Figure 5 is shown the interdependency of the relevant thermoelectric variables that make the optimization of a thermoelectric material a challenging task. The Seebeck coefficient is typically higher for insulators or semiconductors (with high carrier concentration) while the electrical conductivity increases with the carrier concentration and is maximum for metals. Thermal conductivity increases with carrier concentration (same behaviour is found on the electrical conductivity) and is generally maximum for metals [14].
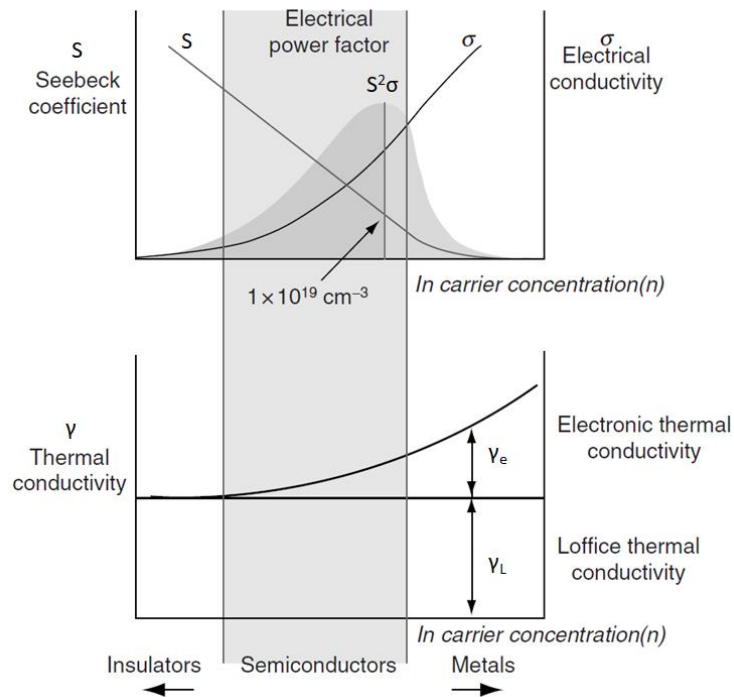

Figure 5. a) Dependence of Seebeck coefficient (S), electrical conductivity (σ) and thermal conductivity (γ) on carrier concentration. **Image adapted with permission from,** [14].

The dependence of the Seebeck coefficient on several variables such as the absolute temperature T_A , carrier density at energy E ($n(E)$), mobility at energy E ($\mu(E)$), the Fermi

energy E_F and electronic charge q_c, is given by the Mott relation [33, 47] and is expressed in Equation (22):

$$S = \frac{\pi^2}{3} \frac{\kappa_B}{q_c} \kappa_B T_A \left(\frac{1}{n} \frac{dn(E)}{dE} + \frac{1}{\mu} \frac{d\mu(E)}{dE} \right)_{E=E_F} \tag{22}$$

Typical values of the Seebeck coefficient for insulators, semiconductors and metals are 10, 200 and >200 μVK^{-1}, respectively. For an ideal thermoelectric material, the Seebeck coefficient should be larger than 200 μVK^{-1}, meaning that they have the ability to generate high voltages [47]. As observed in Figure 6, and explicitly dictated by Equation (22), the values of the thermoelectric figure of merit (zT) depends strongly with temperature.
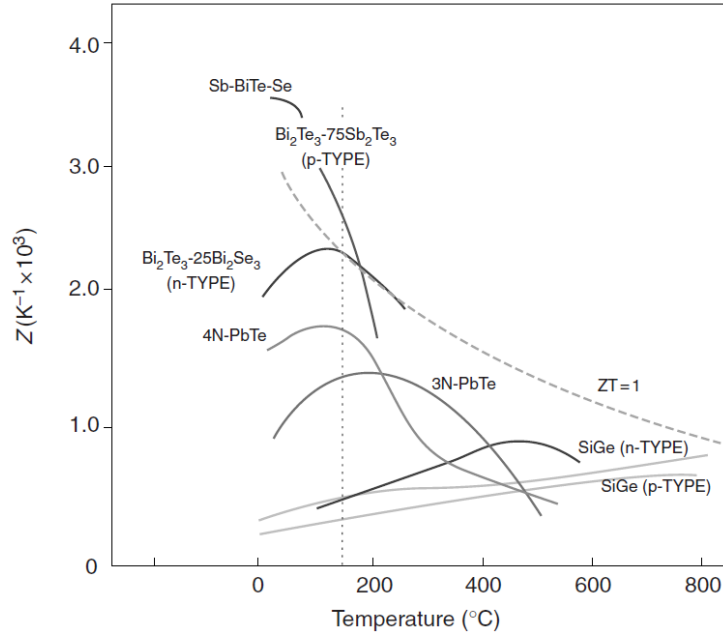

Figure 6. Evolution of thermoelectric figure of merit with temperature for several thermoelectric materials. **Image taken with permission from,** [14].

The electrical conductivity should be properly evaluated as it controls the thermoelectric response of the thermoelectric material. Equation (23) shows the electrical conductivity of a semiconductor as a function of the carrier concentration and mobility:

$$\sigma = e(\mu_e \cdot n + \mu_h \cdot p) \tag{23}$$

14

where e, μ_e, μ_h, n and p represent the electron charge, electron mobility, hole mobility, density of electrons and density of holes, respectively. Figure 7 summarizes the variation of electrical conductivity for different materials (insulators, semiconductors and metals).

Metals exhibit the highest electrical conductivity ranging from 10^3 to 10^6 $(\Omega.cm)^{-1}$ followed by semiconductors (10^{-7} to 10^3 $(\Omega.cm)^{-1}$) and insulators (10^{-20} to 10^{-7} $(\Omega.cm)^{-1}$).
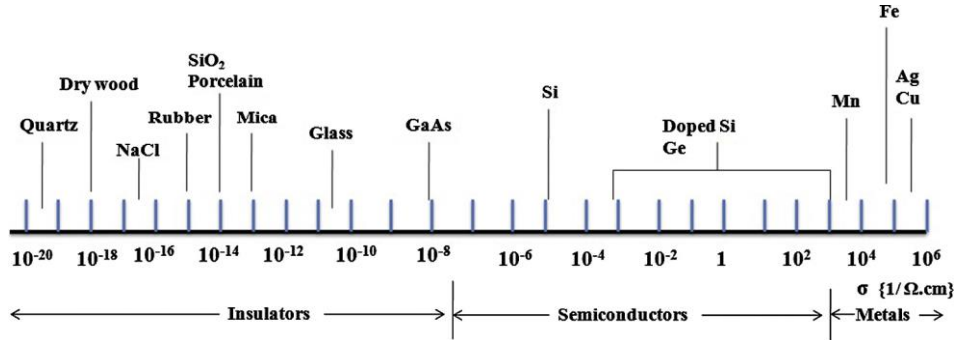
Figure 7. Electrical conductivity at room temperature for different material types. **Image taken with permission from,** [47].

The generation and control of the thermal conductivity is also important. For semiconductors the net thermal conductivity is the sum of two contributions (charge carriers and phonons) [45, 47]:

$$\gamma = \gamma_c + \gamma_{lattice} \tag{24}$$

Where γ_c is the charge-carrier thermal conductivity and $\gamma_{lattice}$ is the lattice thermal conductivity. It should be noted the existence of a relationship between the thermal and electrical conductivities given by the Wiedemann-Franz law (see Equation (25)). This law states that for metals (at temperatures above 0 K) the ratio of carrier thermal conductivity (γ) to electrical conductivity (σ) is directly proportional to temperature [48].

In Equation (25), L represent the Lorentz number that, for metals, is equal to approximately $2.45e^{-8}V^2K^{-2}$ [47, 48].
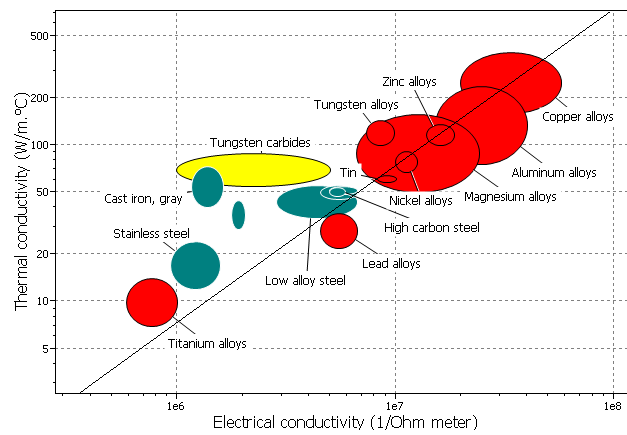
$$\frac{\gamma_c}{\sigma} = LT \tag{25}$$

On the other hand, the lattice contribution to the thermal conductivity is given by:

$$\gamma_{lattice} = D \cdot C_p \cdot \rho \tag{26}$$

where D is the thermal difusivity, C_p the specific heat and ρ the material density.

Figure **8.** shows the relation between electrical conductivity and thermal conductivity for an specific set of metallic alloys.

Figure 8. Relation between thermal conductivity and electrical conductivity for a set of metallic alloys. **Image taken with permission from,** [49].

4. Structural effects on the thermoelectric response

The internal structure of the thermoelectric material can influence its thermoelectric response [46]. Thus, in recent years and with the advance of nanotechnology, a new generation of thermoelectric materials arises based on low-dimensional materials and nanocomposites [50]. In this context, the performance of new thermoelectric materials increased significantly due to the improved thermoelectric characteristics of those nano and/or mesoscale modified materials, in comparison with bulk or macro materials [51]. Also, in the context of bulk

materials, the effect of material grain size on thermoelectrical properties has been addressed [20, 52-54].

Gau *et al.* [20] evaluated the influence of grain size length on the Seebeck coefficient of bulk $CoSb_3$, showing that that the Seebeck coefficient decreases with increasing grain size, with very small variation for a grain size larger than 2 μm (Figure 9).

.
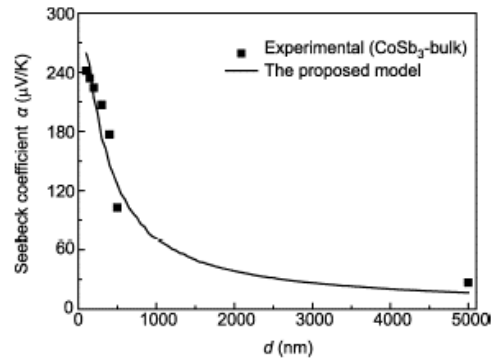
Figure 9. Theoretical prediction and experimental validation of the variation of the Seebeck coefficient with grain size for bulk $CoSb_3$ at T=300K. **Image taken with permission from,** [20].

Kuo *et al.*, studied [52] the effect of cryomilling on the microstructure and thermoelectrical properties of PbTe bulk material samples and it was reported that with decreasing grain size to nanoscale level the thermal conductivity decreases, the Seebeck coefficient increases and there is no significant changes in the electrical conductivity for all samples. Figure 10 shows the SEM images of the unmilled samples as well as the milled ones for 6 and 9 hours, respectively.
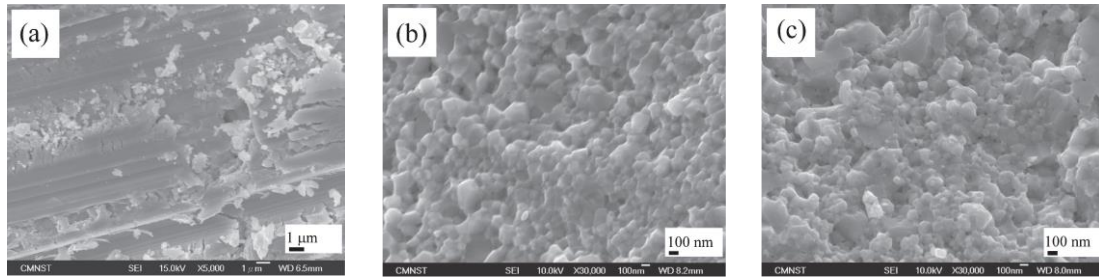
Figure 10. SEM images of bulk PbTe samples unmilled in a); 6h milled in b); and 9h milled in c). **Image taken with permission from,** [52].

The SEM images show that increasing milling time leads to a grain size decrease from 50 μm (unmilled) to a range from 80 nm to 800 nm. The effect on the grain size on the Seebexk coefficient is presented in Figure 11.
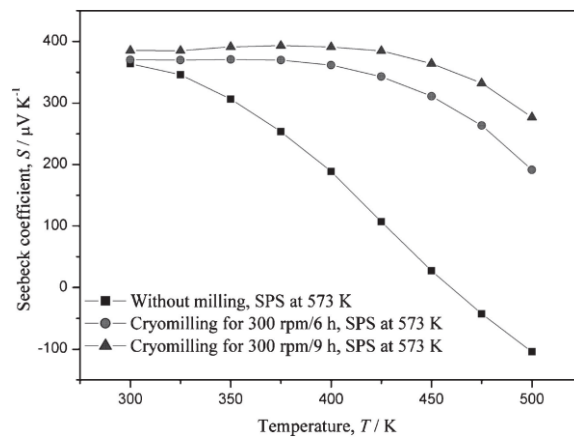
Figure 11. Variation of Seebeck coefficient with temperature for different milling times (grain sizes) for PbTe prepared by spark plasma sintering (SPS) at 573 K. **Image taken with permission from,** [52].

For all samples there is a variation of the Seebeck coefficient with temperature, being the coefficient more stable with temperature for increasing cryomilling time and, consequently, smaller grain sizes.

5. Thermoelectric and thermomagnetic material parameters

In this section special attention will be given to the important material parameters of thermoelectric and thermomagnetic materials.

For thermoelectric materials, the Seebeck coefficient, and other material parameters such as Peltier and Thomson coefficients, can be obtained through the Kelvin relations [11]. Together with the Seebeck coefficient, and as important factors for the characterization of the thermoelectric phenomena, the thermal conductivity and electrical conductivity at room temperature of relevant materials are summarized in Table 1, together with other relevant physical parameters

Table 1. Key parameters for thermoelectricity evaluation of some materials.

Material	Seebeck coefficient (μV.K^{-1})			γ (W.m^{-1}K^{-1})	σ (S.cm^{-1})	Density (kg.m^{-3})	Specific heat (J.kg^{-1}K^{-1})	Figure of Merit (zT)	Ref
	0ºC	27ºC	1000ºC						
Cu	+1.70	+1.84	+7.0	401	0.596 x 10^6	8940	380	1.8x10^{-4}	[47, 55, 56]
Al	-1.6	-1.8	-	237	0.377 x 10^6	2702	900	-	[47, 57, 58]
Ti	-	+3.3	-	21.9	0.0234 x 10^6	4506	520	2.56x10^{-3}	[47, 58]
Ag	+1.38	+1.51	-	429	0.630 x 10^6	10490	235	1x10^{-4}	[47, 57, 58]
Au	+1.79	+1.94	+4.0	317	0.452 x 10^6	19300	128	-	[55, 57, 58]
Pt	-4.45	-5.28	-21.4	71.6	0.0966 x 10^6	21090	130	-	[55, 57, 58]
Brass (Cu50Zn)	-	+0.5 [a]	-	150	0.159 x 10^6	8900	402	-	[55, 59, 60]
Carbon fibre P25 (0pristine – not interlaced)	-	-1.04 [b]	-	640 [d]	4.545 x 10^{3} [d]	2170 [d]	-	-	[61, 62]
Carbon fibre T300 (pristine not intercalated)	-	-6.84 [b]	-	8	0.555 x 10^3	1760	-	-	[61, 62]
Stainless Steel	-	-1.1 [a]	-	15	0.0132 x 10^6	7900	511	-	[55]
AuPt Alloy (75%-25%)		-≈15.0 [e]	-	≈40.0 [c]	≈0.0250 x 10^{6} [c]	≈20000 [c]	-	-	[63]

a) Average over [0, 100] ºC; b) In the [20, 110] ºC temperature range; c) For a temperature equal to 18 ºC; d) Values reported for P120 (Pitch precursor) fibre; e) Seebeck coefficient value relative to pure gold.

By analyzing Table 1 and considering equation (22), element materials on their own do not have the necessary conditions to be used as thermoactive materials being their response to temperature (Seebeck coefficient) lower when compared to alloys.

Table 2 summarizes the thermomagnetic coefficients for several elements. It should be highlighted that it is very difficult to find bibliographical information on thermomagnetic coefficients, in particular, for elemental materials. In fact, the information summarized in Table 2 is related to a paper from P.W. Bridgman [52] dated in 1918.

Table 2. Thermomagnetic material parameters [64]. Electrical quantities are in absolute e.m.u..

Metal	Hall (H)	Ettinghausen (P)	Nernst (N)	Righi-Leduc (S)
	$(x\ 10^{-4})$	$(x\ 10^{-9})$	$(x\ 10^{-4})$	$(x\ 10^{-7})$
Ag	-8.4	-1.65	-1.8	-2.7
Al	-4.0	+1.06	+0.42	-0.62
Cd	+8.8	+2.9	-1.2	+0.89
Co	+24.5	+21.6	+7.8	+1.1
Cu	-5.5	-1.6	-1.9	-2.1
Fe	+87.0	-42.6	-9.5	+5.2
Ni	-29.0	+30.3	+10.0	-2.5
Zn	+7.6	-2.67	-0.73	+1.1
Au	-6.5	-0.96	-1.7	-2.5
Sb	+21900	+1940	+176.0	+20.1
Bi	-63300	+35000	+1780.0	-20.5

On the other hand, information on the thermomagnetic coefficients on metallic alloys is more often reported. Figure 12 is summarized the Nernst coefficient divided by

temperature as a function of the ratio of mobility divided by Fermi energy for metallic alloys.

It is observed a linear trend characterized by $283 \times \frac{\mu_e}{E_F}$.
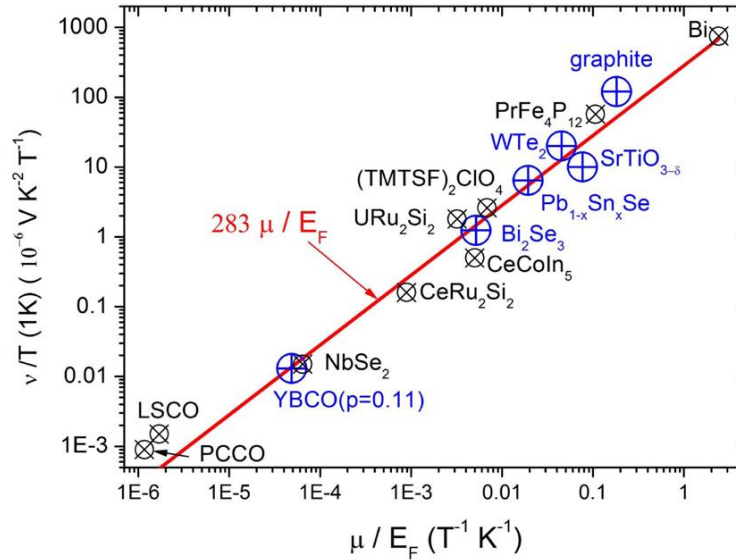
Figure 12. Magnitude of the Nernst coefficient divided by temperature in a variety of metals versus the ratio of mobility to Fermi energy. **Image taken with permission from,** [65].

6. Representative applications

The theoretical and experimental work performed along the years allowed the development and design of different applications for thermoactive materials. They exhibit specific advantages such as direct energy conversion, having low maintenance and long life span, among others [66]. All applications follow the same principle, based on the heat to electricity conversion. The application potential expands in areas such as aerospace [66-76], gas sensors [77-100], flexible applications [101-109], biomedical [104-107, 110-119], and solar powered devices [120-124], among others [125-134]. Some of the devices

used in such applications will be reviewed in this section due to their relevance and potential.

6.1 Aerospace

Thermoactive materials have an important role in the aerospace industry, being intensively used over the years. Depending on the objective of a space mission type or space aircraft they can be needed, to increase performance, or avoided, to reduce measurement noise.

TEGs based with nuclear technology have been used from 1961 with the reported Pb-Te generator capable of generating an electric power of approximately 2.7 W [67]. These generators use mostly the heat provided by the natural decay of plutonium-238 with extreme reliability, being able to perform for several years or even decades. They can be used to provide energy in places with remote access to sunlight where common solar panels do not provide enough energy. Launched in 1997, the Voyager I and II spacecrafts also employ radioisotope TEGs with SiGe thermocouples. They were equipped with 3 generators each of them providing 423 W of power from 7000 W of heat, resulting in an efficiency of approximately 16.55 % when they were first launched [66]. This power tends to decrease slightly over time as a consequence of the decay of plutonium and the degradation of the thermocouples [68]. The most common materials to be used as thermocouples are PbSnTe, PbTe and SiGe and currently the research is focused in the improvement of their performance, in particular with respect to improving electrical properties and decreasing lattice conductivity of such materials, as well as the study of other potential materials [66].

When it comes to missions that require a spacecraft without magnetic interferences, the craft can experience a deteriorated performance due to magnetic fields arising from thermoelectric

sources, which in the beginning were not considered potential sources of magnetic field "contamination". During the extensive magnetic qualification campaign of the individual components of the Absolute Scalar Magnetometer (ASM) (Figure 13) no relevant magnetic perturbation was found, as it was reported an overall precision of 45 pT [69]. However, during the execution of final integration tests of the Swarm mission satellites [70], unexpected thermomagnetic perturbation emerged in the 10 nT range when the heaters from the thermal control of the ASM were activated [71]. Again, and according to [71], magnetic fields originated from thermoelectric currents in a Titanium (Ti) alloy bracket and brass harness lead to the replacement (or removal) of those components during the on-ground satellite test campaign. The original titanium brackets, including the heaters for the thermal control of the ASM, were replaced by Carbon Fibre Reinforced Polymer (CFRP). The hardware upgrade demonstrated efficiency by the reduction of thermomagnetic perturbations to the $20\text{-}30 \pm 5$ pT peak-to-peak range [71]. In mission context, the Swarm satellite operation revealed systematic disagreements between the norm of the Vector Field Magnetometer (VFM) and the magnetic field intensity data obtained from the ASM scalar data [72], namely outside sun-eclipses. In fact, the ASM of the three satellites of the Swarm project suffer for unforeseen magnetic disturbances, soon after launch of Swarm which could not be captured by the traditional in-flight calibration methods [73].
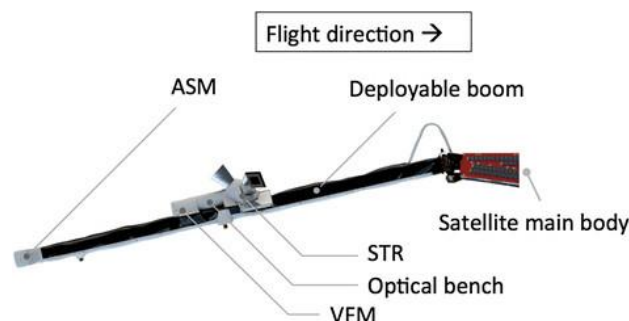

Figure 13. Magnetometer payload setup. **Image taken with permission from,** [74].

Also in Laser Interferometer Space Antenna (LISA) Pathfinder, a demonstration mission to validate important technologies to observe gravitational waves [75], unexpected magnetic fields created by thermal gradients were detected during the development of gold-platinum (AuPt) test mass, that are used to detect gravitational waves through the continuous monitoring of the distance between them by interferometric measurements [76]. However the origin of this magnetic perturbations is not completely understood, the microscopic inhomogeneity and grain boundaries of AuPt alloy could be contributing to the appearance of localized thermal gradients and, consequently, to differences in electric potential as a result of a thermoelectric effect. The appearance of magnetic disturbances or other external disturbances can contribute to an unexpected behaviour of the test masses.

The variation of electrical resistivity ($1/\sigma$) with temperature for a set of aerospace alloys and the variation of thermal conductivity with temperature is represented in Figure 14.
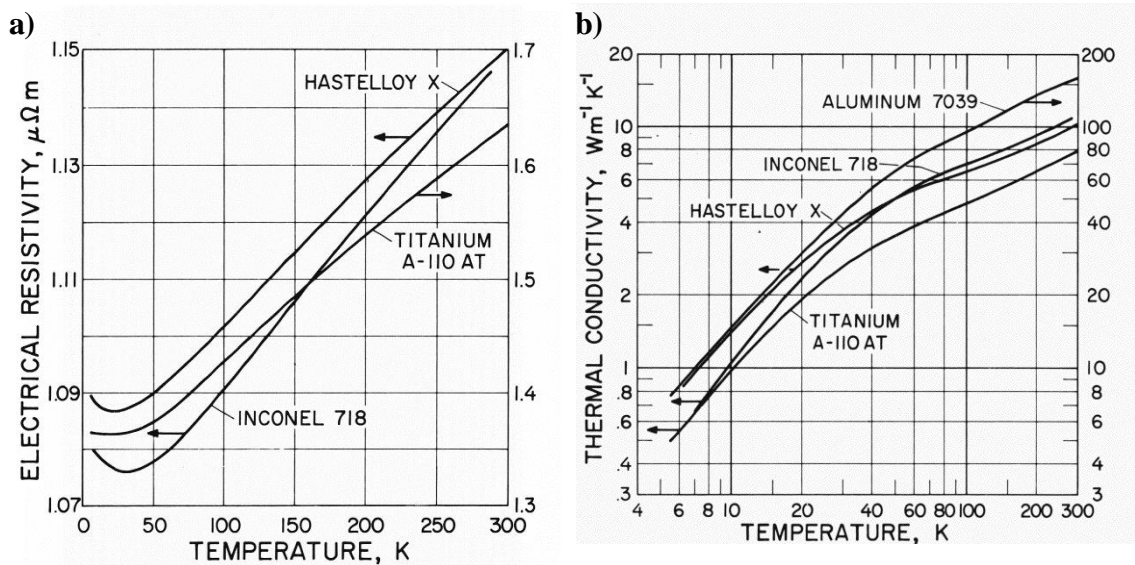
Figure 14. a) Variation of electrical resistivity for Titanium (A-110 AT) and Nickel-Chromium (Inconel 718) and Nickel-Chromium-Iron-Molybdenum (Hastelloy X) alloys. b) Variation of thermal conductivity for Titanium (A-110 AT), Nickel-Chromium (Inconel 718) and Nickel-Chromium-Iron-Molybdenum (Hastelloy X) alloys. **Image taken with permission from,** [99].

The different materials exhibit very similar high electrical resistivity and behavior with a minimum value for the electrical resistivity at approximately 25 K and with a variation of only 10-20 % between 0 K and 300 K. This fact could be of significant importance since the electrical resistivity is inversely proportional to the Seebeck coefficient and thus, these materials will show small variations with increasing temperature and by consequence less disturbance will be produced in the aerospace measurements arising from the thermoelectric phenomena.

6.2 Sensing and self-powered sensors

Thermoelectric materials are already widely used in many sensing areas such as, gas and temperature sensing. They are used for gas sensing in lower gas concentrations with a good accuracy, often with deviations below 1 % [95, 96]. This is very important since some gases percentages as small as 1 volume percentage (vol. %) in air can be fatal. Thermoelectric materials are usually used in the detection of hydrogen (H_2) [77-88, 91, 92, 97] but also in the detection of other gases such as carbon monoxide (CO) [93, 98], carbon dioxide (CO_2) and oxygen (O_2) [89, 90], among others [100]. Regarding hydrogen detection, Kim *et al*. [77] designed and built a hydrogen sensor composed by a Bi_2Te_3 thermoelectric film deposited in a silicon wafer by pyramidical electrodeposition and platinum catalytic nanofibers produced by electrospinning and sputtering. The thermoelectric film has a fundamental role in the improvement of hydrogen detection, maximizing hydrogen flow and with an output voltage with platinum nanofiber 18 times higher than with a platinum thin film. Shin *et al.* [78] also developed a hydrogen sensor based in a platinum thin film in a nickel oxide surface. The sensor detected concentrations from 0.025 to 10 vol. % in an air atmosphere with a good linear response. Later, it was also developed a similar sensor with improved performance by the modification of the catalyst surface by exposing it to Hexamethyldisiloxane (HMDS),

enhancing hydrogen selectivity against methanol from 1.9 to 3.4 at 100 ℃ [79]. Tajima *et al.* [80] and Qiu *et al.* [81, 82] reported something similar by combing a SiGe thermoelectric thin films with platinum. The first ones reported a consumption of 0.34 W at 100 ℃ detecting concentrations between 0.01 and 3 vol. % with a good linearity between the signal and gas concentration and exhibiting high selectivity and the second ones with operating temperatures ranging from 29 to 140 ℃ with a recovery time smaller than 50 s and a detection from 100 ppm to 10 ppm. Choi *et al.* [83] and Shin *et al.* [84] built micro-thermoelectric hydrogen sensors with a Pt/Al_2O_3 ceramic catalyst and a SiGe thermoelectric layers reporting increasing response with the ceramic catalyst when compared with the sensor without Al_2O_3 showing as well a linear relation between hydrogen concentration and output voltage at room temperature. Zhang *et al.* [85] suggested a Bi_2Te_3 thermoelectric sensor covered with a Pt/ activated carbon clothes (ACC) catalyst layer operative at hydrogen concentrations ranging from 0.5 to 3 vol. % and at temperatures below 160 ℃ exhibiting a better response at room temperature when compared to higher temperatures with a recovering response < 60 s due to oxidation reactions that occur above 160 ℃. Matsumiya *et al.* [86] designed a Pt/NiO/ Al_2O_3 sensor and studied the effect of the platinum catalyst thickness and morphology suggesting that the catalytic activity of the sensor increased with increasing thickness with a saturation above 60 nm and decreasing with increasing grain size. Huang *et al.* [87] built a highly selective sensor working at room temperature with bismuth telluride couples and a Pt/γ-Al_2O_3 with good linearity for hydrogen concentrations higher than 0.5 vol.% and high recovery time of 30 s. Already with a prototype, Nishiboru *et al.* [88] developed a catalytic sensor to be used in hydrogen infrastructure systems. The prototype consisted in a micro thermoelectric hydrogen sensor (micro-THS) integrated in a flameproof metal cap and pressure proof cap. The final device presented good linearity between the signal and gas concentrations in air atmosphere for hydrogen concentrations ranging from 10 ppm to 40 000 ppm. When testing the sensor

performance for a year, it was noticed that it was sensible to humidity and some degradation occurred, and so a more robust and reliable module is necessary. For oxygen detection, Rettig *et al.* [89] also developed a sensor based in α-Fe_2O_3 with a sensibility of 85 $\mu V.K^{-1}$ and a time response of 6.4 s for a temperature of 580 ºC. A thick-film electrolyte sensor based in zirconia was designed by Röder-Roith *et al.* [90]. This sensor was non-geometry dependent and had no cross- sensitivity, revealing high selectivity to oxygen when compared to other gases with a good linearity between the oxygens partial pressure and output voltage. Goto *et al.* [93] developed a sensor for CO detection based of Au/SnO_2-Co_3O_4 catalysts capable of detecting the gas with excess levels as small as 0.1 vol. %. Also for the detection of CO_2, Kasyutich *et al* [94] developed a sensor based on a thermoelectrically-cooled quantum cascade laser. This sensor was tested both in ambient air and in gas lines with concentrations from 2.25 ppm to 108.15 ppm.

Other interesting characteristic of thermoelectric devices is their flexibility, which makes them very effective to harvest the dissipated/wasted heat to supply electricity for low energy consuming devices such as wearable electronics, wireless communication units and sensors [101-109]. Iezzi *et al.* [101], developed a TEG based wireless sensor from low cost materials (screen printed silver and nickel) with a power of 308 μW at a ΔT of 127 K, sufficient to power a temperature sensing circuit with wireless communication capabilities. After an initial charging process of 4 hours, the TEG was able to power an RFduino microcontroller for 10 min sending reading of the temperature every 30 s via Bluetooth at the same time. We *et al.* [102] fabricated a screen printed inorganic thermoelectric thick film using the organic conducting polymer poly (3, 4-ethylenedioxythiophene): poly (styrenesulfonate) (PEDOT:PSS), exhibiting great flexibility and high output power density of 1.2 $mW.cm^2$ with a ΔT of 50 K. Seo *et al.* [103] suggested a flexible and detachable multi sensor for the measurement of fluid temperature and dynamics using structured thermoelectric materials,

namely, bismuth telluride and copper deposited in a polyethylene terephthalate (PET) substrate. This sensor was tested in water exhibiting elevated resolution sensing of temperature (< 0.19 K) and velocity (< 0.03 cm.s^{-1}), and its performance was validated with theoretical simulation with COMSOL^{TM}. Finally, a device for real time fluid temperature and dynamics scalable sensor was developed and tested in flat and curved structures with a self-power production of 42 μm.cm^{-2}. In the development of a wireless sensor node Kim *et al*. [109] used flexible TEGs self-powering with dimensions 140 x 113 mm^2, capable of harvesting 272 mW of energy in an heat pipe upon heating up to 70 ^{o}C. These TEGs were capable of powering a wireless sensor node to monitor humidity, ambient temperature, heat pipe temperature and volatile compounds and CO_2 concentrations.

6.3 Biomedical

In the development of biomedical devices, thermoelectric materials are still in their initial stages, but are proving to be a possible new route as an alternative tool to the ones currently available [118]. Currently, implantable biomedical devices are either battery powered or have the need of powering wires which could led to problems related to the development of infections and the need for more frequent surgeries for its replacement. So, energy harvesting devices provide a longer lifetime, comfort and safety. One of the most efficient energy harvesting devices are TEGs, providing energetic autonomy [119], as briefly mentioned in the previous section. For implantable medical devices, the required power usually ranges between μW and mW [110]. Lay-Ekaukille *et al*. [111], produced a TEG capable of harvest energy from the warmth of the human body to supply a hearing device. Leonov *et al*. [112], investigated some hybrid wearable energy harvesters base of a TEG and photovoltaics that power two autonomous medical devices: an electroencephalography (EEG) system and an electrocardiography (ECG) system in a shirt. Qing *et al*. [104, 105] modelled a flexible ink

based (nano-carbon bismuth telluride) film TEG for human body sensing, capable of producing an output voltage of 0.2 $\mu V.cm^{-2}$. Cheng *et al*. [106] developed a flexible thermoelectric sponge based of cellulose to be used as a wearable pressure sensor and energy harvester. The sponge was composed by cellulose nanofibers, polyethyleneimine (PEI) and PEDOT:PSS capable of generating 0.3 mV at 291 K when in contact with the skin with a temperature of 307 K. Francioso *et al*. [107] designed biometric sensor with a flexible generator compose of Sb_2Te_3/Bi_2Te_3 thin films deposited in a kapton substrate. This, low cost, maintenance free, energy autonomous and wearable device, with a ΔT of 15 K, is capable of generating an output voltage of 16 mV. Another interesting class of sensing devices are breath sensors based on thermoelectric devices to evaluate colonic flora based on hydrogen concentration. Nishibori *et al*. [113] developed a system capable of detecting small amount of H_2 (4-103 ppm) coexisting with various gases such as methane and carbon monoxide, being also unaffected to humidity. More recently, Goto *et al*. [114] built a breath gas monitoring sensor by using SiGe as thermoelectric material and $Pt/\alpha-Al_2O_3$ as the catalyst, operating at different temperatures between 100 ℃ and 150 ℃ and tested as proof of concept.

It is to be noticed that, thermoelectric and thermomagnetic phenomena hold great promise for the development of biomedical devices that need to evaluate magnetic field and currents which require low voltages to operate, e.g. in brain research and organs activity monitoring [112, 115], pacemakers [116] and implants [117], among others [118].

6.5 Solar cells

Photovoltaic devices have been and are an area of increasing interest for solar energy conversion. However, most devices only absorb a certain wavelength from the sunlight spectrum. This unabsorbed radiation converts very fast into heat, resulting in a waste heat energy of approximately 40 % [135]. The implementation of TEGs into these devices can help

not only with the absorption of more radiation but also support the prevention of overheating through their direct heat conversion.

On the other hand, the works on solar cells composed of TEGs report limited efficiency related with problems regarding the concentration of heat in the thermoelectric elements and the difficulty to have materials with the capability of endure high temperatures (for implementation in aerospace). For example, Kraemer *et al.* [120], modelled a flat-panel solar TEG technology with an efficiency of 4.6 % with 1 kW.m^{-2} solar conditions. They have also modelled and optimized an earth based solar TEG [121] as a cost effective competitor to offer electricity and hot water. Baranowski *et al.* [122], developed a model to predict the efficiency of a solar TEG stating that with the current thermoactive materials available is possible to obtain an efficiency of 14.1 % with a ΔT of 900 K.

The current solution for such limitations in order to improve efficiency would be hybrid solar cells. Lee *et al.* [123], developed one of these hybrid devices using PEDOT:PSS in the form of a film with high conductivity as the TEG with a resistance of 1.36 Ω for a film with 12.30 µm thick without inducing any hybridization loss, making this material suitable for organic based hybrid photovoltaic devices . Da *et al.* [124] built a theoretical model that takes into account the spectrum reflection loss of the photovoltaic hybrid cell by using a moth-eye nanostructured surface and therefore supressing reflection. They tested both space and terrestrial illuminating conditions, with an increase of efficiency of 3.9 % and 4.72 %, respectively, when compared to a planar geometry.

6.6 Other applications

For automotive energy consumption, thermoelectric devices can be used to convert heat to electricity, improving its efficiency by preventing the dissipation as waste heat to the surrounding environments [125, 128-130]. For example, Hsiao *et al.* [125], have designed and

simulated a module from thermoelectric generators and a cooling system to enhance the efficiency of an internal combustion engine showing results with a maximum power of 51.13 mW.cm^{-2} with a ΔT of 290 K, presenting a better performance on the engine than on the radiator. They also have high potential for their use in developing countries due to their reliability and low maintenance, making their use possible as electricity producers, stoves, and other devices [126, 131-134].

On the other hand, has referenced before, it has to be noted that implementation of thermomagnetic devices is still a challenge, mostly due to their high cost and low efficiency [66]. Nonetheless, some progress has been made. As an example, Joshi *et al*. [127] describe a multi-physics numerical model for a thermomagnetic energy harvester composed of a combination of hard and soft magnets, of Neodymium and Gadolinium, respectively, on a vibrating beam structure and two opposing heat transfer surfaces where the maximum power obtained was 318 μW with a load resistance of 100 kΩ.

7. Conclusions

Thermoelectic and thermomagnetic effects are effects that offer a large possibility of applications and that must be also considered as a source of potential problems in special high sensitivity cases and environments. Precise simulation models have to be developed considering the several parameters affecting thermoelectric and thermomagnetic response, such as grain size and interphase and interface effects, so that novel material and geometries can be developed with improved and tailor made performance. With the numerous and disruptive applications introduced and discussed, it is shown the elevated potential and versatility of the implementation of thermoactive materials. Even though, the implementation of the thermoactive materials and thermoelectric devices can still be a challenge in some areas,

such as in biomedical applications, their potential cannot be set aside once their efficiency is improved.

References

1. Rohrman, F.A., *The Theory of the Properties of Metals and Alloys (Mott, N. F.; Jones, H.).* Journal of Chemical Education, 1937. **14**(2): p. 99.

2. Varlamov, A.A. and A.V. Kavokin, *Prediction of thermomagnetic and thermoelectric properties for novel materials and systems.* Epl (Europhysics Letters), 2013. **103**(4): p. 47005.

3. Seebeck, T.J., *Ueber die magnetische Polarisation der Metalle und Erze durch Temperaturdifferenz.* Annalen der Physik, 1826. **82**(3): p. 253--286.

4. Apertet, Y., et al., *A note on the electrochemical nature of the thermoelectric power.* European Physical Journal Plus, 2016. **131**(4).

5. Zhang, X. and L.-D. Zhao, *Thermoelectric materials: Energy conversion between heat and electricity.* Journal of Materiomics, 2015. **1**(2): p. 92-105.

6. Abrikosov, A.A., *Fundamentals of the Theory of Metals*. 2017: Dover Publications.

7. Metzger, R.M., *The Physical Chemist's Toolbox*. 2012: Wiley.

8.   Goupil, C., et al., *Thermodynamics of Thermoelectric Phenomena and Applications.* Entropy, 2011. **13**(8): p. 1481.

9.   Kretzschmar, K.M. and D.R. Wilkie, *Use of Peltier effect for simple and accurate calibration of thermoelectric devices.* Proceedings of the Royal Society Series B-Biological Sciences, 1975. **190**(1100): p. 315-321.

10.   Apertet, Y. and C. Goupil, *On the fundamental aspect of the first Kelvin's relation in thermoelectricity.* International Journal of Thermal Sciences, 2016. **104**: p. 225-227.

11.   Callen, H.B., *The Application of Onsager's Reciprocal Relations to Thermoelectric, Thermomagnetic, and Galvanomagnetic Effects.* Physical Review, 1948. **73**(11): p. 1349-1358.

12.   S. Yushanov, L.G., J. Crompton and K. Koppenhoefer, *Multiphysics Analysis of Thermoelectric Phenomena*. 2011: COMSOL Conference.

13.   Goldsmid, H.J., *Introduction to Thermoelectricity*. 2016: Springer Berlin Heidelberg.

14.   Rowe, D.M., *Thermoelectrics Handbook: Macro to Nano*. 2005: CRC Press.

15.   Behnia, K., *Fundamentals of Thermoelectricity*. 2015: OUP Oxford.

16.   Dong, H.C., B. Wen, and R. Melnik, *Relative importance of grain boundaries and size effects in thermal conductivity of nanocrystalline materials.* Scientific Reports, 2014. **4**.

17.   Zhou, S., et al., *Multiscale modeling of Thermoelectric Generators for conversion performance enhancement.* International Journal of Heat and Mass Transfer, 2015. **81**(Supplement C): p. 639-645.

18.   Mortazavi, B. and T. Rabczuk, *Multiscale modelling of heat conduction in all-MoS2 single-layer heterostructures.* RSC Advances, 2017. **7**(18): p. 11135-11141.

19.   Wu, Y., et al., *Numerical simulations on the temperature gradient and thermal stress of a thermoelectric power generator.* Energy Conversion and Management, 2014. **88**: p. 915-927.

20.   Gao, Y., Y. He, and L. Zhu, *Impact of grain size on the Seebeck coefficient of bulk polycrystalline thermoelectric materials.* Chinese Science Bulletin, 2010. **55**(1): p. 16-21.

21.   Trivedi, V., et al., *Microstructure and doping effect on the enhancement of the thermoelectric properties of Ni doped Dy filled CoSb3 skutterudites.* Sustainable Energy & Fuels, 2018. **2**(12): p. 2687-2697.

22.   Buschow, K.H.J., *Concise Encyclopedia of Magnetic and Superconducting Materials.* 2005: Elsevier Science.

23.   Schröder, K. and M. Otooni, *Effect of magnetic fields on the absolute Seebeck coefficient and the resistivity of thermocouple wires.* Journal of Physics D: Applied Physics, 1971. **4**(10): p. 1612-1616.

24.   Murata, M., et al., *Magnetic-Field Dependence of Thermoelectric Properties of Sintered Bi90Sb10 Alloy.* Journal of Electronic Materials, 2016. **45**(3): p. 1875-1885.

25.   Homm, G., et al., *Effects of interface geometry on the thermoelectric properties of laterally microstructured ZnO-based thin films.* physica status solidi (a), 2012. **210**(1): p. 119-124.

26.   Wang, M., et al., *Effects of Interface and Grain Boundary on the Electrical Resistivity of Cu/Ta Multilayers.* Journal of Materials Science & Technology, 2009. **25**(5): p. 699-702.

27.   Sharp, J.W., S.J. Poon, and H.J. Goldsmid, *Boundary Scattering and the Thermoelectric Figure of Merit.* physica status solidi (a), 2001. **187**(2): p. 507-516.

28.   Hicks, L.D. and M.S. Dresselhaus, *Effect of quantum-well structures on the thermoelectric figure of merit.* Physical Review B, 1993. **47**(19): p. 12727-12731.

29.   Vashaee, D. and A. Shakouri, *Improved Thermoelectric Power Factor in Metal-Based Superlattices.* Physical Review Letters, 2004. **92**(10): p. 106103.

30.   Heremans, J.P., C.M. Thrush, and D.T. Morelli, *Thermopower enhancement in lead telluride nanostructures.* Physical Review B, 2004. **70**(11): p. 115334.

31.   Heremans, J.P., C.M. Thrush, and D.T. Morelli, *Thermopower enhancement in PbTe with Pb precipitates.* Journal of Applied Physics, 2005. **98**(6): p. 063703.

32.   Medlin, D.L. and G.J. Snyder, *Interfaces in bulk thermoelectric materials: A review for Current Opinion in Colloid and Interface Science.* Current Opinion in Colloid & Interface Science, 2009. **14**(4): p. 226-235.

33.   Heremans, J.P., et al., *Enhancement of thermoelectric efficiency in PbTe by distortion of the electronic density of states.* Science, 2008. **321**(5888): p. 554-557.

34. Polozine, A., S. Sirotinskaya, and L. Schaeffer, *History of development of thermoelectric materials for electric power generation and criteria of their quality.* Materials Research, 2014. **17**: p. 1260-1267.

35. Tripathi, M.N. and C.M. Bhandari, *High-temperature thermoelectric performance of Si–Ge alloys.* Journal of Physics: Condensed Matter, 2003. **15**(31): p. 5359.

36. Wang, X., et al., *Rare earth chalcogenide Ce3Te4 as high efficiency high temperature thermoelectric material.* Applied Physics Letters, 2011. **98**(22): p. 222110.

37. Keshavarz, M.K., et al., *p-Type Bismuth Telluride-Based Composite Thermoelectric Materials Produced by Mechanical Alloying and Hot Extrusion.* Journal of Electronic Materials, 2013. **42**(7): p. 1429-1435.

38. Gürth, M., et al., *Thermoelectric high ZT half-Heusler alloys Ti1−x−yZrxHfyNiSn (0 ≤ x ≤ 1; 0 ≤ y ≤ 1).* Acta Materialia, 2016. **104**: p. 210-222.

39. Cho, H., et al., *Enhancement of thermoelectric properties in CuI-doped Bi2Te2.7Se0.3 by hot-deformation.* Journal of Alloys and Compounds, 2018. **731**: p. 531-536.

40. Wang, H.C., et al., *Enhancement of thermoelectric figure of merit by doping Dy in La0.1Sr0.9TiO3 ceramic.* Materials Research Bulletin, 2010. **45**(7): p. 809-812.

41. Lee, P.-Y., et al., *Enhancement of the thermoelectric performance in nano-/micro-structured p-type Bi0.4Sb1.6Te3 fabricated by mechanical alloying and vacuum hot pressing.* Journal of Alloys and Compounds, 2014. **615**: p. S476-S481.

42. Du, Z., et al., *Effect of Ga alloying on thermoelectric properties of InSb.* Current Applied Physics, 2018. **18**(8): p. 893-897.

43. Saurabh, S., et al., *Effect of nanostructure on thermoelectric properties of La 0.7 Sr 0.3 MnO 3 in 300–600 K temperature range.* Materials Research Express, 2018. **5**(5): p. 055026.

44. Kurosaki, K., et al., *Enhanced Thermoelectric Properties of Silicon via Nanostructuring.* Materials Transactions, 2016. **57**(7): p. 1018-1021.

45. Rowe, D.M., *CRC Handbook of Thermoelectrics.* 2006: CRC Press, Taylor & Francis Group.

46. Li, J.-F., et al., *High-performance nanostructured thermoelectric materials.* Npg Asia Materials, 2010. **2**: p. 152.

47.   Gayner, C. and K.K. Kar, *Recent advances in thermoelectric materials.* Progress in Materials Science, 2016. **83**: p. 330-382.

48.   Kittel, *Introduction to solid state physics, 7th Ed.* 2007: Wiley India Pvt. Limited.

49.   Cambridge, U.o., *Introduction to thermal and electrical conductivity.* [Online] Available: https://www.doitpoms.ac.uk/tlplib/thermal_electrical/printall.php.

50.   Dresselhaus, M.S., et al., *New directions for low-dimensional thermoelectric materials.* Advanced Materials, 2007. **19**(8): p. 1043-1053.

51.   Snyder, G.J. and E.S. Toberer, *Complex thermoelectric materials.* Nature Materials, 2008. **7**: p. 105.

52.   Kuo, C.-H., et al., *Thermoelectric Properties of Fine-Grained PbTe Bulk Materials Fabricated by Cryomilling and Spark Plasma Sintering.* Materials Transactions, 2011. **52**(4): p. 795-801.

53.   Wang, S.F., et al., *Effect of microstructure on the thermoelectric properties of CSD-grown Bi2Sr2Co2Oy thin films.* Chinese Physics B, 2013. **22**(3).

54.   Takashiri, M., et al., *Effect of grain size on thermoelectric properties of n-type nanocrystalline bismuth-telluride based thin films.* Journal of Applied Physics, 2008. **104**(8): p. 084302.

55.   Bentley, R.E., *Handbook of Temperature Measurement Vol. 3: The Theory and Practice of Thermoelectric Thermometry.* 1998: Springer Singapore.

56.   Davis, J.R. and A.S.M.I.H. Committee, *Copper and Copper Alloys.* 2001: ASM International.

57.   Kasap, S., *Thermoelectric effect in metals: thermocouples.* 2018.

58.   Lide, D.R., *CRC Handbook of Chemistry and Physics, 84th Edition.* 2003: Taylor & Francis.

59.   TIBTECH and innovations, *Properties table of Stainless steel, Metals and other Conductive materials.* 2011, Available: http://www.tibtech.com/conductivity.php. [Accessed 25 10 2017].

60.   Engineers and Edge, *Specific Heat Capacity of Metals Table Chart.* 2017, [Online] Available: https://www.engineersedge.com/materials/specific_heat_capacity_of_metals_13259.htm.

61.   Chung, D.D.L., *Applied Materials Science: Applications of Engineering Materials in Structural, Electronics, Thermal, and Other Industries.* 2001: CRC Press.

62. Karandikar, P., *Nanotube-containing composite bodies, and methods for making same*. 2006.

63. Darling, A.S., *Gold-Platinum alloys: A critical review of their constitution and properties*. 1962, Johnson Matthey Technology Review. p. 106-111.

64. Bridgman, P.W., *The connections between the four transverse galvanomagnetic and thermomagnetic phenomena*. Physical Review, 1924. **24**(6): p. 644-651.

65. Behnia, K. and H. Aubin, *Nernst effect in metals and superconductors: a review of concepts and experiments*. Reports on Progress in Physics, 2016. **79**(4).

66. Champier, D., *Thermoelectric generators: A review of applications*. Energy Conversion and Management, 2017. **140**(Supplement C): p. 167-181.

67. Shure, L.I. and H.J. Schwartz, *Survey of electric power plants for space applications*, in *Fifty-Eight National Meeting of the American Institute of Chemical Engineers Philadelphia*. 1965: Pensilvania.

68. Rowe, D.M., *Applications of nuclear-powered thermoelectric generators in space*. Applied Energy, 1991. **40**(4): p. 241-271.

69. Jager, T., et al., *SWARM Absolute Scalar Magnetometer Accuracy: Analyses and Measurement Results*. 2010 Ieee Sensors, 2010: p. 2392-2395.

70. Friis-Christensen, E., H. Luhr, and G. Hulot, *Swarm: A constellation to study the Earth's magnetic field*. Earth Planets and Space, 2006. **58**(4): p. 351-358.

71. Jager, T., et al. *Magnetic cleanliness and thermomagnetic effect: Case study of the absolute scalar magnetometer and its environment on swarm satellites*. in *2016 ESA Workshop on Aerospace EMC (Aerospace EMC)*. 2016.

72. Hulot, G., et al., *Swarm's absolute magnetometer experimental vector mode, an innovative capability for space magnetometry*. Geophysical Research Letters, 2015. **42**(5): p. 1352-1359.

73. Toffner-Clausen, L., et al., *In-flight scalar calibration and characterisation of the Swarm magnetometry package*. Earth Planets and Space, 2016. **68**.

74. Vigneron, P., et al., *A 2015 International Geomagnetic Reference Field (IGRF) candidate model based on Swarm's experimental absolute magnetometer vector mode data*. Earth Planets and Space, 2015. **67**.

75. Armano, M., *The LISA Pathfinder Mission*. J. Phys. Conf. Ser, 2015. **610**: p. 1-18.

76. Antonucci, F., et al., *The LISA Pathfinder mission*. Classical and Quantum Gravity, 2012. **29**(12): p. 124014.

77. Kim, S., et al., *Thermochemical hydrogen sensor based on Pt-coated nanofiber catalyst deposited on pyramidally textured thermoelectric film.* Applied Surface Science, 2017. **415**: p. 119-125.

78. Shin, W., et al., *Thermoelectric gas sensor for detection of high hydrogen concentration.* Sensors and Actuators B: Chemical, 2004. **97**(2): p. 344-347.

79. Sawaguchi, N., et al., *Enhanced hydrogen selectivity of thermoelectric gas sensor by modification of platinum catalyst surface.* Materials Letters, 2006. **60**(3): p. 313-316.

80. Tajima, K., et al., *Micromechanical fabrication of low-power thermoelectric hydrogen sensor.* Sensors and Actuators B: Chemical, 2005. **108**(1): p. 973-978.

81. Qiu, F., et al., *Investigation of thermoelectric hydrogen sensor based on SiGe film.* Sensors and Actuators B: Chemical, 2003. **94**(2): p. 152-160.

82. Qiu, F., et al., *Miniaturization of thermoelectric hydrogen sensor prepared on glass substrate with low-temperature crystallized SiGe film.* Sensors and Actuators B-Chemical, 2004. **103**(1-2): p. 252-259.

83. Choi, Y., et al., *Combustor of ceramic Pt/alumina catalyst and its application for micro-thermoelectric hydrogen sensor.* Applied Catalysis A: General, 2005. **287**(1): p. 19-24.

84. Shin, W., et al., *Planar catalytic combustor film for thermoelectric hydrogen sensor.* Sensors and Actuators B: Chemical, 2005. **108**(1): p. 455-460.

85. Zhang, J., et al., *Preparation and characteristics of Pt/ACC catalyst for thermoelectric thin film hydrogen sensor.* Sensors and Actuators B: Chemical, 2007. **128**(1): p. 266-272.

86. Matsumiya, M., et al., *Nano-structured thin-film Pt catalyst for thermoelectric hydrogen gas sensor.* Sensors and Actuators B-Chemical, 2003. **93**(1-3): p. 309-315.

87. Huang, H., et al., *Thermoelectric hydrogen sensor working at room temperature prepared by bismuth-telluride P-N couples and Pt/gamma-Al2O3.* Sensors and Actuators B-Chemical, 2008. **128**(2): p. 581-585.

88. Nishibori, M., et al., *Robust hydrogen detection system with a thermoelectric hydrogen sensor for hydrogen station application.* International Journal of Hydrogen Energy, 2009. **34**(6): p. 2834-2841.

89.   Rettig, F. and R. Moos, *α-Iron oxide: An intrinsically semiconducting oxide material for direct thermoelectric oxygen sensors.* Sensors and Actuators B: Chemical, 2010. **145**(2): p. 685-690.

90.   Roder-Roith, U., et al., *Thick-film solid electrolyte oxygen sensors using the direct ionic thermoelectric effect.* Sensors and Actuators B-Chemical, 2009. **136**(2): p. 530-535.

91.   Shin, W., et al., *Hydrogen-selective thermoelectric gas sensor.* Sensors and Actuators B: Chemical, 2003. **93**(1): p. 304-308.

92.   Sawaguchi, N., et al., *Effect of humidity on the sensing property of thermoelectric hydrogen sensor.* Sensors and Actuators B: Chemical, 2005. **108**(1): p. 461-466.

93.   Goto, T., et al., *CO sensing properties of Au/SnO2–Co3O4 catalysts on a micro thermoelectric gas sensor.* Sensors and Actuators B: Chemical, 2016. **223**: p. 774-783.

94.   Kasyutich, V.L. and P.A. Martin, *A CO2 sensor based upon a continuous-wave thermoelectrically-cooled quantum cascade laser.* Sensors and Actuators B-Chemical, 2011. **157**(2): p. 635-640.

95.   Rettig, F. and R. Moos, *Direct thermoelectric gas sensors: Design aspects and first gas sensors.* Sensors and Actuators B: Chemical, 2007. **123**(1): p. 413-419.

96.   Rettig, F. and R. Moos, *Temperature-modulated direct thermoelectric gas sensors: thermal modeling and results for fast hydrocarbon sensors.* Measurement Science and Technology, 2009. **20**(6).

97.   Shin, W., et al., *Fabrication of thermoelectric gas sensors on micro-hotplates.* Sensors and Actuators B-Chemical, 2009. **139**(2): p. 340-345.

98.   Xu, T., et al., *Thermoelectric carbon monoxide sensor using Co-Ce catalyst.* Sensors and Actuators B-Chemical, 2008. **133**(1): p. 70-77.

99.   Hust, J.G., D.H. Weitzel, and R.L. Powell, *Thermal conductivity, electrical resistivity, and thermopower of aerospace alloys from 4 to 300 K.* Journal of Research of the National Bureau of Standards Section a-Physics and Chemistry, 1971. **A 75**(4): p. 269-+.

100.   Wiegartner, S., et al., *Thermoelectric hydrocarbon sensor in thick-film technology for on-board-diagnostics of a diesel oxidation catalyst.* Sensors and Actuators B-Chemical, 2015. **214**: p. 234-240.

101. Iezzi, B., et al., *Printed, metallic thermoelectric generators integrated with pipe insulation for powering wireless sensors.* Applied Energy, 2017. **208**(Supplement C): p. 758-765.

102. We, J.H., S.J. Kim, and B.J. Cho, *Hybrid composite of screen-printed inorganic thermoelectric film and organic conducting polymer for flexible thermoelectric power generator.* Energy, 2014. **73**(Supplement C): p. 506-512.

103. Seo, B., et al., *Flexible-detachable dual-output sensors of fluid temperature and dynamics based on structural design of thermoelectric materials.* Nano Energy, 2018. **50**: p. 733-743.

104. Qing, S.W., et al., *Characteristics and parametric analysis of a novel flexible ink-based thermoelectric generator for human body sensor.* Energy Conversion and Management, 2018. **156**: p. 655-665.

105. Qing, S.W., et al., *Design of flexible thermoelectric generator as human body sensor.* Materials Today-Proceedings, 2018. **5**(4): p. 10338-10346.

106. Cheng, H., et al., *Flexible cellulose-based thermoelectric sponge towards wearable pressure sensor and energy harvesting.* Chemical Engineering Journal, 2018. **338**: p. 1-7.

107. Francioso, L., et al., *Flexible thermoelectric generator for ambient assisted living wearable biometric sensors.* Journal of Power Sources, 2011. **196**(6): p. 3239-3243.

108. Zhu, W., Y. Deng, and L.L. Cao, *Light-concentrated solar generator and sensor based on flexible thin-film thermoelectric device.* Nano Energy, 2017. **34**: p. 463-471.

109. Kim, Y.J., et al., *High-performance self-powered wireless sensor node driven by a flexible thermoelectric generator.* Energy, 2018. **162**: p. 526-533.

110. Hannan, M.A., et al., *Energy harvesting for the implantable biomedical devices: issues and challenges.* Biomedical Engineering Online, 2014. **13**.

111. Lay-Ekuakille, A., et al. *Thermoelectric generator design based on power from body heat for biomedical autonomous devices*. in *2009 IEEE International Workshop on Medical Measurements and Applications*. 2009.

112. Vladimir Leonov, et al., *Hybrid Thermoelectric–Photovoltaic Generators in Wireless Electroencephalography Diadem and Electrocardiography Shirt.* Journal of Electronic Materials, 2010. **39**(9): p. 1674-1680.

113. Nishibori, M., et al., *Sensing performance of thermoelectric hydrogen sensor for breath hydrogen analysis.* Sensors and Actuators B-Chemical, 2009. **137**(2): p. 524-528.

114. Goto, T., et al., *Heat transfer control of micro-thermoelectric gas sensor for breath gas monitoring.* Sensors and Actuators B-Chemical, 2017. **249**: p. 571-580.

115. Kim, C.S., et al., *Self-Powered Wearable Electrocardiography Using a Wearable Thermoelectric Power Generator.* ACS Energy Letters, 2018. **3**(3): p. 501-507.

116. Bhatia, D., et al., *Pacemakers charging using body energy.* Journal of pharmacy & bioallied sciences, 2010. **2**(1): p. 51-54.

117. Jadhav, O.S., et al. *Design of a thermoelectric generator for electrical active implants.* in *MikroSystemTechnik 2017; Congress.* 2017.

118. Chen, A. and P. K. Wright, *Medical Applications of Thermoelectrics.* 2012. p. 26-1.

119. Torfs, T., et al. *Wearable Autonomous Wireless Electro-encephalography System Fully Powered by Human Body Heat.* in *2008 IEEE Sensors.* 2008.

120. Kraemer, D., et al., *High-performance flat-panel solar thermoelectric generators with high thermal concentration.* Nature Materials, 2011. **10**: p. 532.

121. Kraemer, D., et al., *Modeling and optimization of solar thermoelectric generators for terrestrial applications.* Solar Energy, 2012. **86**(5): p. 1338-1350.

122. Baranowski, L.L., G.J. Snyder, and E.S. Toberer, *Concentrated solar thermoelectric generators.* Energy & Environmental Science, 2012. **5**(10): p. 9055-9067.

123. Lee, J.J., et al., *All organic-based solar cell and thermoelectric generator hybrid device system using highly conductive PEDOT:PSS film as organic thermoelectric generator.* Solar Energy, 2016. **134**: p. 479-483.

124. Da, Y., Y. Xuan, and Q. Li, *From light trapping to solar energy utilization: A novel photovoltaic-thermoelectric hybrid system to fully utilize solar spectrum.* Energy, 2016. **95**: p. 200-210.

125. Hsiao, Y.Y., W.C. Chang, and S.L. Chen, *A mathematic model of thermoelectric module with applications on waste heat recovery from automobile engine.* Energy, 2010. **35**(3): p. 1447-1454.

126. Champier, D., et al., *Thermoelectric power generation from biomass cook stoves.* Energy, 2010. **35**(2): p. 935-942.

127. Keyur, B.J. and P. Shashank, *Multi-physics model of a thermo-magnetic energy harvester.* Smart Materials and Structures, 2013. **22**(5): p. 055005.

128. Brignone, M. and A. Ziggiotti, *Impact of novel thermoelectric materials on automotive applications.* AIP Conference Proceedings, 2012. **1449**(1): p. 493-496.

129. Magnetto, D. and G. Vidiella, *Reduced energy consumption by massive thermoelectric waste heat recovery in light duty trucks.* AIP Conference Proceedings, 2012. **1449**(1): p. 471-474.

130. Frobenius, F., et al., *Thermoelectric Generators for the Integration into Automotive Exhaust Systems for Passenger Cars and Commercial Vehicles.* Journal of Electronic Materials, 2016. **45**(3): p. 1433-1440.

131. Najjar, Y.S.H. and M.M. Kseibi, *Thermoelectric stoves for poor deprived regions – A review.* Renewable and Sustainable Energy Reviews, 2017. **80**(Supplement C): p. 597-602.

132. Nuwayhid, R.Y., D.M. Rowe, and G. Min, *Low cost stove-top thermoelectric generator for regions with unreliable electricity supply.* Renewable Energy, 2003. **28**(2): p. 205-222.

133. Rinalde, G.F., et al., *Development of thermoelectric generators for electrification of isolated rural homes.* International Journal of Hydrogen Energy, 2010. **35**(11): p. 5818-5822.

134. O'Shaughnessy, S.M., et al., *Field trial testing of an electricity-producing portable biomass cooking stove in rural Malawi.* Energy for Sustainable Development, 2014. **20**: p. 1-10.

135. Nelson, J., *The Physics of Solar Cells*. 2003: Imperial College Press.